



Deep Learning Assisted Microwave Photonic Dual-Parameter Sensing

Xiaoyi Tian , Luping Zhou , Senior Member, IEEE, Liwei Li , Member, IEEE, Giorgio Gunawan ,
Linh Nguyen , and Xiaoke Yi , Member, IEEE

Abstract—The combination of optical microresonators and the emerging microwave photonic (MWP) sensing has recently drawn great attention, whereas its multi-parameter sensing capability mainly relies on adopting multiple resonance modes. By incorporating deep learning (DL) into MWP sensing, we propose a new sensing paradigm, which has the simplified design, reduced fabrication requirement, and the capability of sensing more than one parameter. The MWP interrogation transforms the spectral response of a single optical resonance (SOR) that can be at arbitrary coupling conditions into the variations of the zero-transmission profile of microwave signals, providing improved interrogation resolution regardless of the resonance parameters. A DL unit is used to exploit the raw interrogation output to simultaneously estimate the target measurands. As the proof-of-concept demonstration, simultaneous temperature and humidity sensing using a SOR is conducted, where the convolutional neural tangent kernel (CNTK) is used as the DL model to reduce the demand for experimental data. The established CNTK-DL model consistently outperforms the support vector regression model that relies on handcrafted features and demonstrates an over 2-fold higher estimation accuracy with the laser drift interference and a lower mean absolute error in the presence of strong noise, showing the power of DL for boosting MWP sensing.

Index Terms—Deep learning, machine learning, microwave photonics, optical resonators, optical signal processing, sensors.

I. INTRODUCTION

OPTICAL microresonators, such as microrings, microrods, and microspheres, can strongly enhance the light-matter interaction by confining the resonant light at specific wavelengths through total internal reflection along the sidewalls of a microscale cavity. Optical microresonator based sensors

Manuscript received 29 January 2023; revised 10 May 2023; accepted 11 July 2023. Date of publication 18 July 2023; date of current version 8 September 2023. The work was supported by the Australian Research Council. (Corresponding author: Xiaoke Yi.)

Xiaoyi Tian, Liwei Li, and Xiaoke Yi are with the School of Electrical and Information Engineering, The University of Sydney, Sydney, NSW 2006, Australia, and also with the University of Sydney Nano Institute (Sydney Nano), The University of Sydney, Sydney, NSW 2006, Australia (e-mail: xiaoyi.tian@sydney.edu.au; liwei.li@sydney.edu.au; xiaoke.yi@sydney.edu.au).

Luping Zhou and Linh Nguyen are with the School of Electrical and Information Engineering, The University of Sydney, Sydney, NSW 2006, Australia (e-mail: luping.zhou@sydney.edu.au; linh.n@sydney.edu.au).

Giorgio Gunawan is with the School of Aerospace, Mechanical and Mechatronic Engineering, The University of Sydney, Sydney, NSW 2006, Australia (e-mail: ggun7030@uni.sydney.edu.au).

Color versions of one or more figures in this article are available at <https://doi.org/10.1109/JSTQE.2023.3296385>.

Digital Object Identifier 10.1109/JSTQE.2023.3296385

have been attracting great attention [1], [2]. Their remarkable properties, including the label-free detection and real-time monitoring capabilities and the exceptional sensitivity to any environmental perturbation that can influence the optical mode distribution, coupled with their diverse fabrication platforms and compatibility with the existing chip-based technologies, have led to a broad range of applications [3], [4], [5], [6], [7], [8].

Conventionally, the interrogation of resonant mode changes relies on directly measuring the optical transmission using an optical spectrum analyzer. This is simple but of limited speed, especially when high resolution is needed, and the performance largely depends on the fabrication accuracy of optical microresonator devices [9], [10], [11], [12], [13], [14]. In the pursuit of achieving high speed and high resolution to meet the ever-increasing demand in modern sensor networks, the Internet of Things, and the frontiers in medical and biochemical fields, microwave photonics (MWP), which has been bringing together and benefiting the two worlds of microwave engineering and photonics [15], [16], [17], [18], [19], has been applied into optical sensing in recent years [20], [21]. Different MWP interrogation schemes have been proposed for optical microresonators. The basic idea is to transfer the resonant wavelength shift of optical microresonators in the optical domain into the frequency changes in the microwave domain, where fast and precise measurements are easier to conduct [9], [10], [11], [12]. With the recent advances in photonic integration, which have propelled MWP to a new height by allowing enriched functionality in a dramatically reduced footprint [22], the MWP sensors using integrated devices are promised to be a preferred solution in various high-demanding sensing scenarios. However, the related research effort on the on-chip MWP sensing mainly centers on single-parameter sensing, while the achievement of sensing more than one parameter, which is often required or even indispensable in real-life applications, is still challenging. Along with the variations of the measurands of interests, the undesired perturbations can also be encoded in the optical resonant mode changes, affecting the sensing selectivity. The ability to effectively distinguish different factors is thus vital to achieving accurate and reliable sensing with no ambiguity. Conventional approaches to realizing optical multi-parameter sensing rely on the usage of multiple resonator devices or resonance modes with different sensitivities [9], [23], which increases the complexity of the design, implementation, and interrogation of the sensors. This challenge becomes increasingly pronounced as the required number of resonance modes multiplies. It is, therefore,

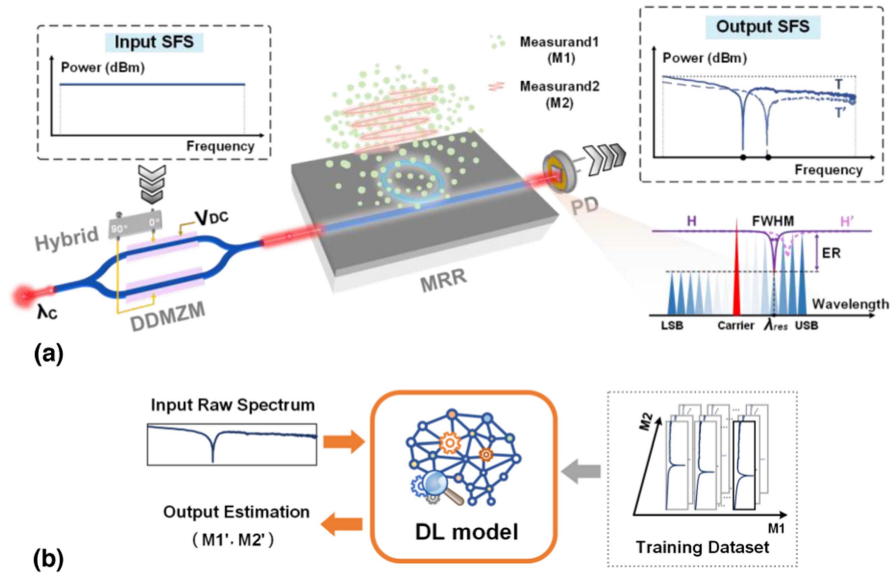


Fig. 1. Proposed new MWP sensing scheme consists of (a) the high-resolution MWP interrogation system for the optical microresonator sensors, which uses a DDMZM to map the single optical resonance responses, including the resonance wavelength shift and the variations of ER and FWHM, in the optical transmission of a MRR into the zero-transmission profile of the SFS, where H and H' are the optical transmissions before and after the measurands change and T and T' are the corresponding SFS transmissions, respectively, and (b) the DL processing of the raw interrogation output, where the DL model automatically extracts the optimal feature representations and is capable of generating the accurate estimation the measurands of interest (M1' and M2') after being sufficiently trained.

necessary to find a new way to enable the MWP sensors to simultaneously detect more than one measurand. Recently, deep learning (DL) has gained ever-increasing attention, as it allows computational models consisting of multiple processing layers to learn to automatically extract optimal feature representations from the raw input for making accurate decisions, even for highly complex problems [24], [25], [26], [27], [28], [29], [30], [31], [32], [33]. It has shown great promises to directly decouple the combined response to different measurands [26], [27], [28], [29], [30]. In comparison with the traditional machine learning (ML) approaches which require handcrafted input [34], [35], [36], the excellent capabilities of DL make it a promising tool to process the interrogation results by automatically recognizing and learning the optimal informative feature representations, rather than solely relying on handcrafting features, for complex mapping [37], [38], [39]. To date, however, to our best knowledge, the DL has not been applied in emerging MWP sensing.

In this article, by combining MWP sensing with DL for the first time, we propose a new MWP sensing paradigm using a single optical resonance (SOR), which has the minimum requirement for the design and fabrication of the optical microresonator sensor and the capability of simultaneously sensing more than one measurand of interest. Through the MWP sideband processing, the spectral response of the SOR to the measurands of interest can be transformed into the zero-transmission profile of the interrogation microwave signals with high resolution. The interrogation output is then directly used as the input for DL processing, where multiple processing layers automatically extract optimal feature representations and achieve accurate simultaneous prediction of the measurands of interest through supervised training. As a proof-of-concept, we experimentally demonstrate the achievement of simultaneous sensing of temperature and

relative humidity (RH) via DL of the MWP interrogation output of a SOR of a generic silicon-on-insulator (SOI) microring resonator (MRR) top-coated with the hygroscopic polymethyl methacrylate (PMMA). The convolutional neural tangent kernel (CNTK) that approximates a convolutional neural network with infinite layer width and is amiable to small datasets is adopted to establish the DL model to reduce the demand for a large amount of experimental data. In comparison with the ML model based on support vector regression (SVR) and two handcraft features extracted from the interrogation output, the DL-assisted MWP sensor consistently shows superior performance, demonstrating a nearly 2-fold and 3-fold higher estimation accuracy with and without the interference of laser drift, respectively, and remains a lower mean absolute error (MAE) in a high noise level. These results demonstrate the superiority of MWP sensing assisted by DL and boost the microresonator for multi-parameter sensing.

II. PRINCIPLES AND METHODS

A. Principle of Operation

Fig. 1(a) depicts the schematic diagram of the high-resolution MWP interrogation system for the optical microresonator sensors in our proposed new sensing approach using only a SOR. The proposed scheme is compatible with any optical microresonator. Here, a standard all-pass MRR, which consists of simply a cavity waveguide and a bus waveguide, is used as an example. The optical transmission profile of a SOR of the MRR at arbitrary coupling conditions is continuously interrogated with high speed and high resolution by using a swept-frequency signal (SFS) modulated onto the excitation light in a dual-drive Mach Zehnder

modulator (DDMZM) via an electrical 90-degree hybrid coupler. By conducting the MWP sideband processing of the modulated light, the transmitted SFS constantly exhibits an ultradeep spectral notch with a sharp tip, indicating the SOR responses to the measurand changes with greatly enhanced resolution. The raw SFS transmission is later used as the direct input for DL processing which enables the simultaneous prediction of more than one measurand of interest.

For the MRR with a self-coupling coefficient of r and a cavity length of L , its optical field transmission, H , with respect to the wavelength of λ and the effective index of n_{eff} can be expressed as [40]

$$H = \frac{a - re^{-i\theta}}{1 - ra e^{i\theta}} e^{i(\pi+\theta)} \quad (1)$$

where a is the single-pass amplitude transmission that reflects the transmission loss in the cavity, and θ is defined as $\theta = \frac{2\pi}{\lambda} n_{eff} L$. Each resonance mode thus corresponds to an optical power transmission dip at the resonance wavelength, λ_{res} , with the notch depth or extinction ratio (ER) equal to

$$ER = \frac{(a+r)^2(1-ar)^2}{(a-r)^2(1+ar)^2} \quad (2)$$

The full width at half maximum (FWHM) of notch width is given by

$$FWHM = \frac{(1-ra)\lambda_{res}^2}{\pi n_g L \sqrt{ra}} \quad (3)$$

where n_g is the group index. When the laser wavelength, λ_C , is placed close to the selected SOR for sensing at the longer wavelength side, as the SFS-modulated optical field, E_m , transmits in the MRR, the optical notch of the SOR will then be scanned by the upper or lower sideband (USB or LSB), consequently resulting in a transmission dip of the SFS. Fig. 1(a) shows an example of using the USB in MWP interrogation. The instantaneous intensity of the transmitted SFS after the photodetector (PD) can be expressed as [9]

$$I^2 = \frac{1}{2} \mathcal{R}^2 P_C \left\{ P_{LSB} + P'_{USB} + 2\sqrt{P_{LSB}P'_{USB}} \cos \Delta\varphi \right\} \quad (4)$$

where \mathcal{R} is the responsivity of the PD, P_C , and P_{LSB} are the initial optical power of the optical carrier and LSB, respectively. P'_{USB} represents $P_{USB}|H(\lambda_{USB})|^2$, which is the instantaneous USB power, P_{USB} , being filtered by the SOR power transmission dip at the wavelength position of λ_{USB} . $\Delta\varphi$ is the phase difference between the two photocurrent terms resulting from the carrier beating with USB and LSB, respectively, which is dependent on the phase transmission of the SOR and adjustable by the DC bias of DDMZM. The changes of different measurands of interest can lead to a combined variation in the spectral line shapes of the SOR. Through the MWP sideband processing by tailoring the optical power and phase profiles of the optical components in (4) via tuning the DC bias voltage of the modulator, the superposed responses of the SOR, which can have arbitrary coupling states and parameters, can be transformed into the variations of an ultra-deep notch in the SFS transmission spectrum with high resolution.

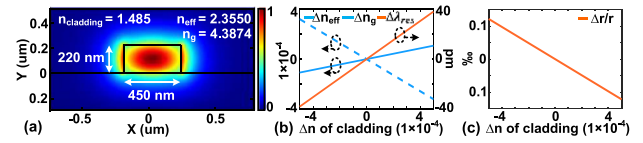


Fig. 2. (a) Simulated cross-section view of the optical field distribution of light transmitted in a standard SOI waveguide shows the strong evanescent waves on the waveguide surface that intimately interact with the top claddings; (b) The variation of the refractive index of top cladding (Δn) results in the change of effective index (Δn_{eff}) and group index (Δn_g) and hence the distinct shift of resonance wavelength ($\Delta \lambda_{res}$); (c) The simulated change of self-coupling coefficient (Δr) of a straight directional coupler as the cladding refractive index varies.

The output of the MWP interrogation is used as the input of the DL for learning and estimation, as shown in Fig. 1(b). The SFS transmission spectrum is measured at various measurand conditions in the target sensing area to establish the DL-based estimation model. The acquired raw spectra labeled with the ground-truth measurand values then comprise the dataset to train the DL model, where the raw spectrum composed of a length of point transmission directly functions as the input layer without experiencing any pretreatment. In the supervised training, the DL neural network containing multiple hidden layers automatically extracts high-level features from the raw spectrum and compares the resulting estimated measurand values in the output layer against the ground truth. Errors are then used to adjust the network coefficients and hyperparameters in the direction of achieving better estimation accuracy. This process occurs over and over through the training dataset until the model has been fitted appropriately with the optimal parameters. Once the DL model is established, the different target measurands of interest can be accurately and simultaneously estimated with the MWP interrogation output of the SOR. In this way, the high-sensitivity and high-resolution MWP sensing of more than one parameter is achieved, which has the minimum requirement on the design and fabrication of the optical microresonator sensor probe.

Fig. 2(a) presents the simulated optical mode field distribution in the cross-section of the SOI waveguide. A finite-difference eigenmode (FDE) solver (Ansys Lumerical) was adopted to numerically calculate the TE mode optical electric field distribution within cross-section area of the waveguide. The simulation was conducted at a wavelength of 1550 nm, with the silicon waveguide dimensions set to 450 nm in width and 220 nm in height, and the refractive index of the top cladding layer fixed at 1.485. As the results indicate, the optical mode field of the transmitted light distributes throughout both the waveguide core and the cladding layers. Thus, any environmental changes that can perturb the optical mode field, especially those as evanescent waves along the waveguide surface, will cause the optical mode indices to vary. Fig. 2(b) shows the changes of n_{eff} and n_g of the simulated optical mode at 1550 nm and the consequent resonance wavelength shift, when the refractive index of the top cladding, $n_{cladding}$, undergoes a variation. Therefore, by using the MRR as the sensor, a tiny index change can be transformed into a distinct resonance wavelength shift. In the meantime, as shown by the simulation results of the self-coupling coefficient of a straight directional coupler which uses the same SOI

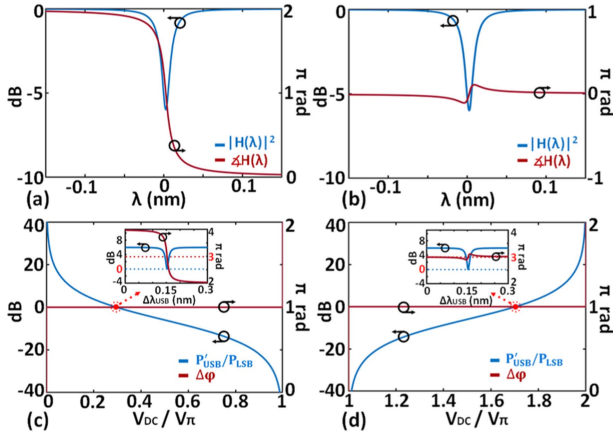


Fig. 3. Optical sideband processing via the DC bias voltage. The simulated power and phase transmission of (a) over-coupled and (b) under-coupled resonant modes show the integer number of π rad phase changes at the resonance wavelength. The simulated power ratio between the USB filtered by the SOR (P'_{USB}) and the LSB (P_{LSB}) and the concurrent $\Delta\varphi$ at different DC bias conditions show that there is always a DC bias voltage in the first and second $V\pi$ range for the (c) over-coupled and (d) under-coupled SOR, respectively, to create the zero transmission. The insets show the instantaneous sideband power ratio and $\Delta\varphi$ as the USB sweeps through the resonance wavelength at the corresponding optimal DC bias condition.

waveguide geometry and has a coupling length of 15 μm and a gap distance of 300 nm in Fig. 2(c), r in (1) is also varying with the optical index of the cladding. Given that the optical indices are wavelength dependent [41], along with the resonance wavelength shift, the overall resonance line shape, therefore, also responds with altered characteristics, such as the ER and FWHM, as indicated by (2) and (3).

Fig. 3 shows the simulated power ratio between P'_{USB} and P_{LSB} and the concurrent $\Delta\varphi$ at different DC bias voltages, when the USB sweeps through the resonance wavelength of an over-coupled (Fig. 3(a)) and under-coupled (Fig. 3(b)) resonance mode, respectively. Since the optical phase transmission at the resonance wavelength is always equal to the integer number of π rad, as shown in Fig. 3(c) and (d), there always exists one DC bias point in the first and second $V\pi$ (half-wave voltage) range to allow the transmitted SFS in (4) for the over-coupled and under-coupled SOR, respectively, to satisfy the following conditions

$$P_{LSB} = P'_{USB} \quad (5a)$$

$$\cos\Delta\varphi = -1 \quad (5b)$$

Therefore, a zero transmission of the SFS ($I^2 = 0$) can always be created regardless of the coupling state of SOR, via automatically controlling the DC bias voltage of the DDMZM [42]. The zero transmission is manifested as the ultradeep dip in the SFS transmission spectrum, where the dip location and spectral line shape are subject to the concurrent resonance wavelength and the original optical resonance line shape. Overall, based on the MWP sideband processing technique, the wavelength position of the selected SOR, which can be at arbitrary coupling states, can be continuously interrogated by locating the zero-transmission point of the SFS. The spectral profile at the

output of MWP interrogation output, which contains the sharp tip of the ultradeep spectral notch enabling the high interrogation resolution, is used as the input of the DL model for measurand prediction.

B. Deep Learning Model

As a proof-of-concept, the proposed DL-assisted MWP sensing scheme using a SOR is validated in the case of simultaneous sensing of temperature and humidity by using a SOI MRR, top-coated with hygroscopic PMMA, as the on-chip sensor probe. Due to the high thermal-optic coefficient of silicon [43] and the humidity-sensitive refractive index of PMMA [44], the transmitted optical resonance modes in the MRR are thus sensitive to the environmental temperature and RH level. The MWP interrogation of the selected SOR of the MRR was carried out at a series of different temperature and humidity conditions to obtain sufficient transmission spectra to comprise the dataset for DL processing and model testing. To reduce the high demand for training data, CNTK [45], [46], [47], which approximates a convolutional neural network with infinite layer width and has been demonstrated to be suitable for small dataset problems [45], is adopted to build the DL model. CNTK is a kind of kernel method that works by transforming input from the original dimension space into a higher dimensional space and searching for an optimal linear function, which may be a highly nonlinear function in the original space, to make the prediction. Therefore, the CNTK allows the DL of transmission spectra with a much lower number of parameters.

The approximation of infinite-width neural networks as kernels depends on three conditions: over-parameterization, proper initialization of parameters, and a sufficiently small learning rate [46]. Given these conditions, as the neural network model becomes over-parameterized, the weight changes are observed to decrease proportionally. The weights will hence remain static during the gradient descent optimization process, even if each layer is built with infinite neurons. This unique feature thus allows the infinite-width neural network to be approximated as its Taylor's expansion around the initialized weights, \mathbf{w}_0 , as [48]

$$f(x, \mathbf{w}) \approx f(x, \mathbf{w}_0) + \langle \nabla_{\mathbf{w}} f(x, \mathbf{w}_0), \mathbf{w} - \mathbf{w}_0 \rangle \quad (6)$$

where $f(x, \mathbf{w})$ refers to the neural network function, \mathbf{w} represents weights, x stands for the input, and $\nabla_{\mathbf{w}} f(x, \mathbf{w}_0)$ is the gradient vector at initialization. As the weights are completely static when the network is highly over-parameterized, \mathbf{w}_0 can be considered a constant. (6) is thus simply a linear model of the weights \mathbf{w} . As proved in [46], [49], training such infinite-width neural network by gradient descent is equivalent to conducting kernel regression expressed as

$$f(x) = K(x, \mathbf{D}) \cdot K(\mathbf{D}, \mathbf{D})^{-1} \cdot \mathbf{y}(\mathbf{D}) \quad (7)$$

where x stands for the test data as the input, which can be assigned with a transmission spectrum acquired from the MWP interrogation during the sensing process, $\mathbf{D} = [\hat{x}_1, \dots, \hat{x}_N]^T$, is the training dataset with a size of N , which is implemented with a collection of the transmission spectra acquired by the MWP interrogation of the SOR at N different known conditions of

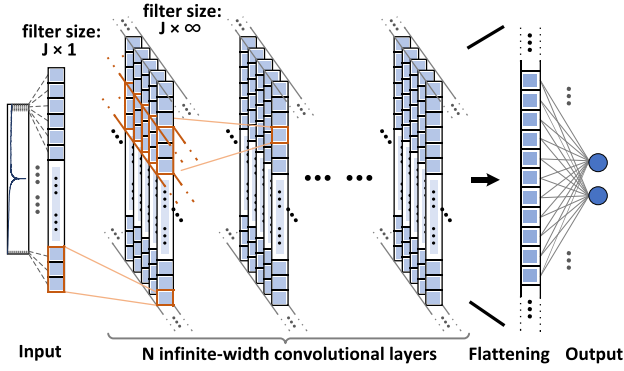


Fig. 4. Experimental CNTK-DL model approximates a convolutional neural network with one input layer of raw transmission spectrum, N infinite-width convolutional layers, and one flattening layer connected to the output estimations of temperature (T) and RH. Each convolutional filter has a size of J, and all the weights and biases are initialized by using the normal distribution.

the measurands of interest throughout the target sensing range, $y(D)$ corresponds to the ground-truth values, i.e., the N known conditions of the measurands of interest, $K(x, x')$ is the kernel function that computes the similarity between two samples, x and x' , by

$$K(x, x') = \langle \nabla_w f(x, w_0), \nabla_w f(x', w_0) \rangle \quad (8)$$

where the gradient vector works as the feature map that transforms the input to higher-dimensional space. The CNTK-DL model thus can be established simply by incorporating the gradient vector function of the convolutional neural network [47], which can be numerically calculated in practical implementations, into (7) and determining the hyperparameters, including only the filter size and the number of layers, through the grid search. As for the weights and biases in each infinite layer, the normal distributions with the variance of 1 and 0 are used, respectively, for the initialization, following an identical configuration in [50]. Fig. 4 depicts the equivalent network structure of the experimental CNTK-DL model. Compared with the deep neural network model, the CNTK-DL model uses multiple layers with infinite width to learn the features of the input, but only has a few parameters to optimize, which, therefore, makes it a more efficient choice for implementing the proposed DL scheme in experiments.

III. EXPERIMENTAL SECTION

A. Device Fabrication and Characterization

The experimental SORs are contributed from SOI MRRs fabricated in the same racetrack shape, as shown in Fig. 5(a), using standard electron-beam lithography technology on a SOI wafer where the silicon waveguides are 220 nm thick and sit on top of a 2 μm buried oxide layer above a 725 μm thick silicon substrate. The bending radius of the curved waveguides is around 27 μm , and the length of the straight waveguides is about 20 μm . The light coupling between the on-chip MRR device and fibers is realized via vertical grating couplers at the end of the bus waveguides. Once fabricated, the SOI MRRs were then spin-coated with the hygroscopic PMMA layer to make

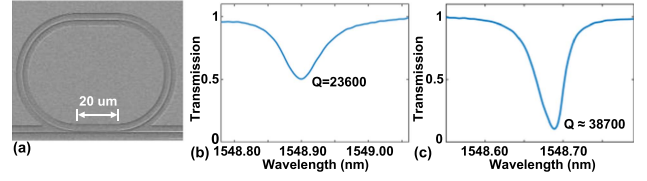


Fig. 5. (a) Scanning electron microscope image shows the racetrack shape of the fabricated SOI MRRs for experiments; Measured optical power transmissions of the MRRs with the waveguide width of (b) 420 nm and (c) 450 nm, respectively.

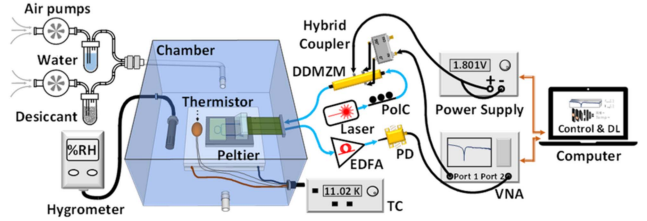


Fig. 6. Schematic of the experimental setup of the proposed SOI based MWP sensor using ML and DL for the simultaneous measurement of temperature and humidity. The PMMA coated SOI MRR sits close to a thermistor on a Peltier, which is connected to a temperature controller and is enclosed in a homemade chamber where the RH level is monitored by a reference hygrometer and adjustable via controlling the wet and dry air flows.

the waveguide cladding index sensitive to the environmental humidity, where the thickness of the PMMA cladding was made to be around 450 nm to envelop the evanescent waves surrounding the MRR waveguides completely. Fig. 5(b) and (c) present the optical transmission of the experimental SORs of PMMA-coated MRR with a 420 nm and a 450 nm waveguide width, respectively, which were measured at room temperature and humidity conditions. Both resonances exhibit a small ER and a wide tip, indicating a limited resolution performance. The 420 nm-SOR has a Q factor of around 23600, while the 450 nm-SOR shows a relatively larger Q factor of around 38700.

B. Experimental Setup

The experimental setup of the simultaneous measurement of temperature and humidity with the proposed DL-assisted MWP sensing scheme using a SOR is illustrated in Fig. 6. The on-chip PMMA-coated SOI MRR, working as the sensor probe, sits close to a thermistor on a Peltier cooler and is enclosed in a homemade chamber made with an inlet and an outlet and proper holes for wires and fibers. The humidity inside the chamber is constantly monitored using a commercially available hygrometer (IC-Center 317) as the humidity reference sensor. The hygrometer has a measurement range of 0-99% RH, a resolution of 0.1% RH, and an accuracy of $\pm 2.5\%$ RH. The interior RH level can be gradually adjusted to and stabilize at the desired value by carefully changing the power of the pumps that bring in the surrounding air into the chamber via tubes filled with water and desiccant. To ensure a reliable reference RH measurement, the MWP interrogation was only performed when the RH level had stabilized, and the concurrent reference RH level was recorded at the same time of the spectrum acquisition. Meanwhile, the temperature variation is achieved by using a temperature controller

(TC) (Newport 325), which detects the thermistor and drives the Peltier cooler. A polarization controller (PoC) is added between the laser source (Keysight, 81960A) and the DDMZM to align the polarization of the light according to the quasi-transverse electric mode of the chip waveguides to minimize the optical loss. The vector network analyzer (VNA) (Keysight, N5234A) is used to generate the SFS, which drives the DDMZM via a 90-degree electric hybrid coupler (Marki microwave, QH0444). The DDMZM bias voltage is supplied by a DC power supply (Keysight, E3632A) which is programmable with a voltage resolution of 1 mV. To compensate for the coupling loss between the on-chip waveguides and optical fibers, an Erbium-doped fiber amplifier (EDFA) is added at the output of the sensor probe before the optical detection in a high-speed PD (u2t). The detected photocurrent is then sent to the VNA, which measures the demodulated SFS and provides the SFS transmission. In practice, the optical modulator, optical microresonator, and PD can be integrated into a single platform to enhance the system compactness and portability [22], while the VNA, which works as a radio frequency transceiver, can be replaced with a compact RF source and power meter to reduce the system volume and cost. The power supply and VNA are connected to a computer that dynamically adjusts the DC bias voltage to maintain the conditions for the high-resolution MWP interrogation during the sensing and processes the acquired interrogation results with ML and DL techniques to enable the sensing of dual parameters.

IV. RESULTS AND DISCUSSIONS

In this section, the performance of the proposed SOR-based MWP sensing scheme using the CNTK-DL model in the simultaneous measurement of temperature and humidity is demonstrated and analyzed. To evaluate the robustness and versatility of the DL-based sensing model, the experiment was carried out in three different scenarios: the SOR-based MWP temperature and humidity sensing under (i) no additional interference, (ii) laser drift, and (iii) strong noise. Laser drift is a common problem in optical systems and critical for long-term operation, while noise resistance is desired for practical deployment. In each experiment, the laser wavelength was kept on the longer-wavelength side of the selected SOR, and 36 spectra in total were acquired in the MWP interrogation of the SOR at six different RH levels, ranging from around 40% RH to around 60% RH in a step of about 4% RH, while the temperature of the MRR chip was set to six equally spaced values, ranging from 22.20 °C to 22.63 °C, via a temperature controller. Each spectrum acquired has a frequency range of 20 GHz and a sample length of 1001, which corresponds to a wavelength resolution of about 0.16 pm at the wavelengths around 1550 nm. The small temperature and humidity increments were adopted to test the interrogation resolution. Although the measurement range of the MWP system demonstrated in this article is limited by the experimental devices and instrument, such as the PD and VNA, it can be extended by utilizing a tunable laser to conduct the multi-channel interrogation via changing the carrier wavelength [51]. The collected transmission spectra labeled with the ground-truth temperature and RH values comprise the datasets for DL

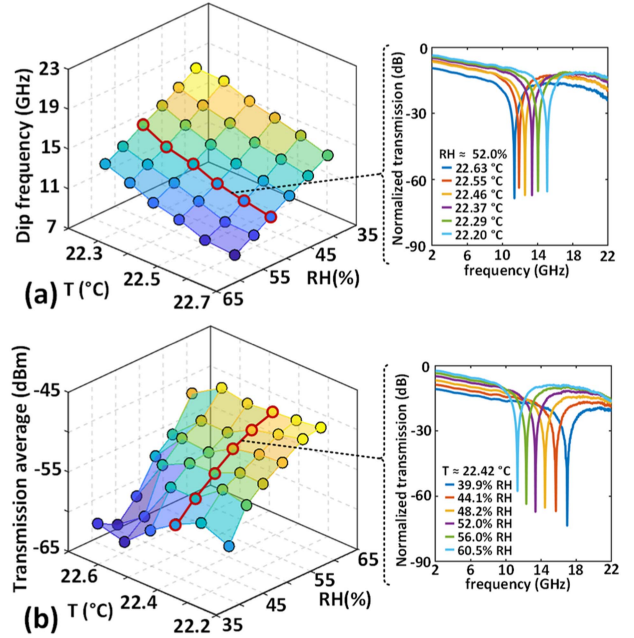


Fig. 7. Flat and rugged distribution of the (a) dip positions and (b) transmission averages extracted from the transmission spectra obtained in Scenario 1, showing their linear and nonlinear relationships with the temperature and RH, respectively. The inset in (a) and (b) presents the transmission spectra (referenced to -20 dBm) collected at a fixed humidity of 52.0% RH and a fixed temperature (T) of 22.42 °C, respectively, which demonstrates the constant high interrogation resolution and varied line shapes at varying temperature and humidity conditions.

processing. For comparison, in parallel with establishing the CNTK-DL model, the SVR-ML model (see Appendix) was also conducted to do the simultaneous sensing of temperature and humidity with the same spectrum datasets and procedures by using two handcrafted spectral features: the transmission dip position and overall average.

A. Data Description

First, as in Scenario 1, the MWP simultaneous sensing of temperature and humidity was carried out without additional interference. The SOR was selected from a fabricated PMMA-coated SOI MRR with a waveguide width of 420 nm. The obtained dataset is named Dataset 1. Two series of spectrum data collected at the same temperature of around 22.42 °C and the same RH level of around 52.0%, respectively, are shown in Fig. 7, where the transmission dip position and overall average extracted from each spectrum data are presented altogether as well. Under different environmental conditions, the transmission dip remains a high rejection ratio of around 50 dB, which is over 47 dB larger than the ER of the selected SOR shown in Fig. 5(b), showing the constant high-resolution performance of the MWP interrogation. When any of the two measurands varies, the transmission spectrum exhibits clear line shape variations, as manifested by the horizontal shifts of dip position and the vertical shifts of the transmission average, which is calculated by the sum of the transmission at every frequency point in the measured transmission spectrum divided by the sample length. As the temperature or humidity level rises, the dip position shifts to the lower frequencies, while the overall transmission

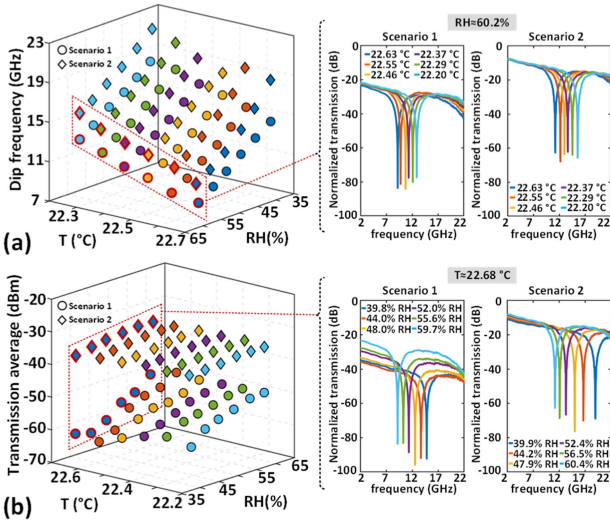


Fig. 8. The (a) dip positions and (b) transmission averages extracted from the transmission spectra collected in Scenario 1 and Scenario 2. The laser drift makes the two spectral features ambiguous and lose validity as individual sensing parameters. The inset in (a) and (b) compares the measured spectra (referenced to -20 dBm) in Scenario 1 and Scenario 2, at the fixed humidity of 60.2% RH and the fixed temperature (T) of 22.68 °C, respectively, showing the clear shape deformations.

average moves in an increasing trend. This nonlinear response of transmission average can be explained by the nonlinear variation of ER, as shown in (2), which constantly changes the average transmitted intensity of SFS via regulating the DC bias voltage of DDMZM according to the matching conditions.

Second, as in Scenario 2, the experiment was conducted with the same 420 nm-SOR and the same experimental conditions as in Scenario 1, but with altered laser wavelength and power. The obtained dataset is named Dataset 2. Fig. 8 compares the spectrum data before and after tuning the laser and the corresponding dip positions and transmission averages. After introducing the laser drift, the high rejection ratio of the transmission dip is still preserved, and the spectrum generally shows a similar response to the measurands. However, at each temperature and humidity condition point, the data shows a clear position deviation in both horizontal and vertical directions. As the laser wavelength drift directly superimposes on the resonance wavelength shift, all the transmission dips appear at a higher frequency, while each of the offsets slightly varies with one another due to the non-zero filtering effect of resonance, in practice, on the optical carrier. At the same time, all the transmission spectra are integrally lifted, to different extents, due to the increased optical power, whereas consequently becoming more overlapped.

In Scenario 3, a SOR selected from a fabricated PMMA-coated SOI MRR with a waveguide width of 450 nm was used in the temperature and humidity sensing experiment in the presence of a high noise level which is realized by decreasing the experimental optical power and also shifting the MWP interrogation window to higher frequencies [9]. The collected spectrum data constitute Dataset 3 and are shown in Fig. 9. Compared with Dataset 1, the total resonance wavelength shift in response to the humidity variation is evidently smaller due to

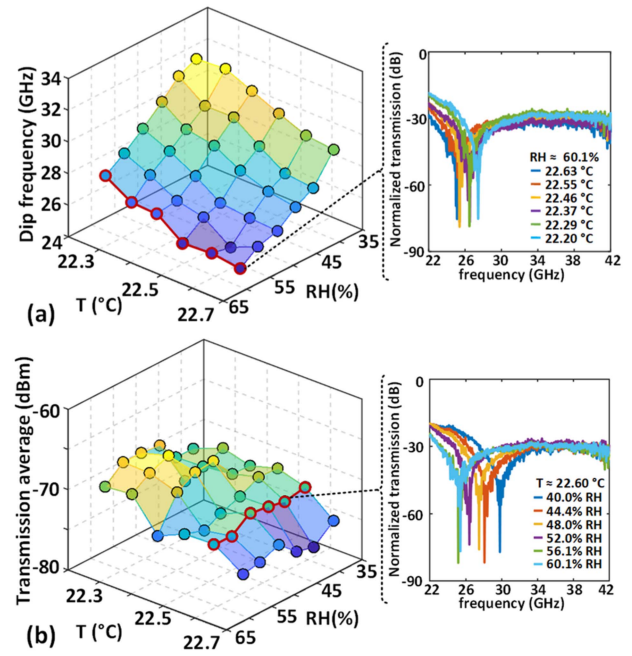


Fig. 9. The (a) dip positions and (b) transmission averages extracted from the transmission spectra obtained in Scenario 3, where there is intentionally induced strong noise interference, exhibit nonlinear variation with respect to the temperature and humidity changes. The inset in (a) and (b) presents the noisy transmission spectra (referenced to -40 dBm) collected at a fixed humidity of 60.1% RH and a fixed temperature (T) of 22.60 °C, respectively.

the wider waveguide width that leads to the less distribution of the transmitted optical mode field in the claddings, although the high rejection ratio of the transmission dip is still retained. The noisy spectra become distorted and blurry and overlap with one another in a wide frequency range. Moreover, the dip position now shifts nonlinearly, and similar to Dataset 2, the change of transmission average at different environment conditions (humidity and temperature) becomes less obvious, showing the deterioration in the signal quality undoubtedly poses challenges to the measurand estimation.

B. Experimental Modeling and Testing Results

As shown in Figs. 7–9, for each dataset, each spectrum data can be identified by a unique pair of dip frequency and transmission average, which indicates that the spectrum data points in each dataset are unambiguous. The 6-fold cross-validation was adopted to establish and test the CNTK-DL model that enables the simultaneous sensing of temperature and humidity using the collected datasets (Datasets 1-3). In each 6-fold cross-validation process, the in-use dataset was first permuted and then split into six subsets. One by one, a subset was selected as the test set, and the rest of the subsets were used as the training sets until all possible combinations were evaluated. In this way, every data point in the dataset was all used as the testing data once. In each validation round, the MAE between the estimated and ground-truth measurand values were calculated. The hyperparameters of both CNTK and SVR models were determined by-way-of grid search in a range of values based on the resulting MAE values during a preliminary validation process. The convolutional layer

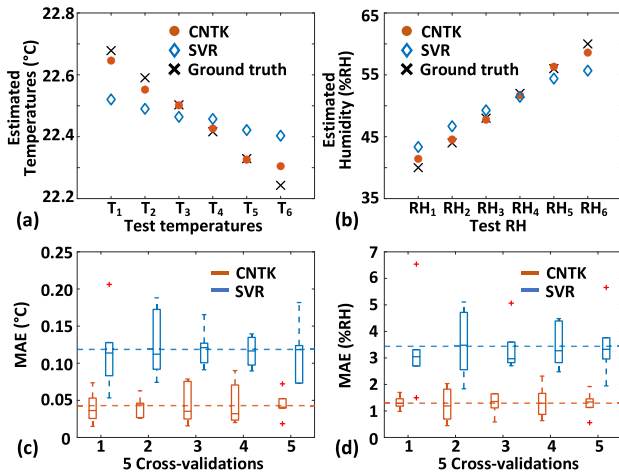


Fig. 10. CNTK-DL model and SVR-ML model were established with Dataset 1, where the median values of the estimation results of CNTK-DL (red dots) are located closer to the ground-truth values (black crosses) than that of the SVR-ML model (blue diamonds) at all the experimental (a) temperature and (b) humidity points. The boxplot of MAE of (c) temperature and (d) humidity estimations in the five 6-fold cross-validations further demonstrate the superiority of DL of the entire spectrum over ML of handcrafted features. The dotted lines indicate the overall average MAE values.

number and filter size of the CNTK-DL model were determined as 8 and 11, respectively, which indicates a low complexity that is beneficial to mitigating overfitting. To ensure a thorough evaluation, five 6-fold cross-validations with different initial permutations were performed with each CNTK-DL and SVR-ML model.

First, the modeling and testing were carried out with Dataset 1. Fig. 10 shows the estimation results by the established CNTK-DL and SVR-ML models. At every testing temperature and humidity condition point, the median estimation values by CNTK-DL are constantly located in closer proximity to the ground truth than that of the SVR-ML model, indicating the better estimation accuracy of the CNTK-DL model. Besides, the total MAEs of the CNTK-DL model for the temperature and humidity estimation in the five 6-fold cross-validations demonstrate a more centralized distribution around small values of around $0.04\text{ }^{\circ}\text{C}$ and 1.30% RH, respectively, while the MAE of the SVR-ML model fluctuates severely in a wide range and results in an overall average MAE being nearly 3-fold worse than that of CNTK-DL model. Although the currently achieved estimation performance is restricted by the size of the experimental dataset, the superiority of DL of the entire raw spectrum over the ML of handcrafted spectral features for sensing is pronounced clearly.

Next, the CNTK-DL and SVR-ML models were established with the combined Dataset 1 and Dataset 2, for the case where there are strong laser drift interferences. The estimation results in the same validation process are shown in Fig. 11. The CNTK-DL model continues to demonstrate a considerably better estimation accuracy with the average estimation MAEs around 2.1-fold smaller than that of the SVR-ML model. Compared with the performance indicated in Fig. 10, the laser drift causes a small deviation to the median prediction by the CNTK-DL model,

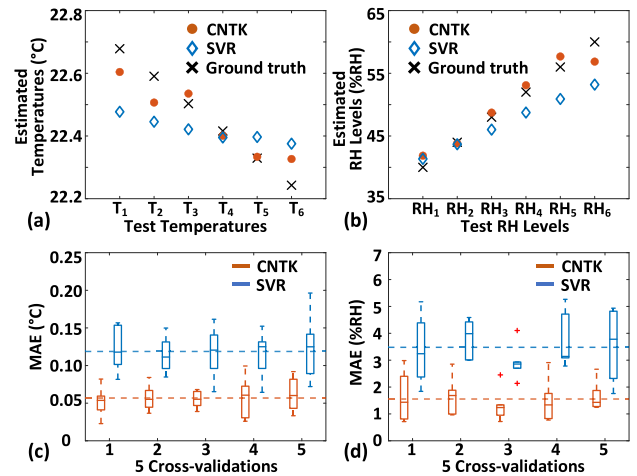


Fig. 11. CNTK-DL model and SVR-ML model were established with combined Dataset 1 and Dataset 2 in the presence of laser drift, where the median values of estimated (a) temperatures and (b) RH levels by CNTK-DL model (red dots) are still located in closer proximity to the ground truth values (black crosses) than that by SVR-ML model (blue diamonds). The boxplot of MAE of (c) temperature and (d) humidity estimations in the five 6-fold cross-validations further demonstrate the resistance of the ML and DL models to the laser drift problem. The dotted lines indicate the overall average MAE values.

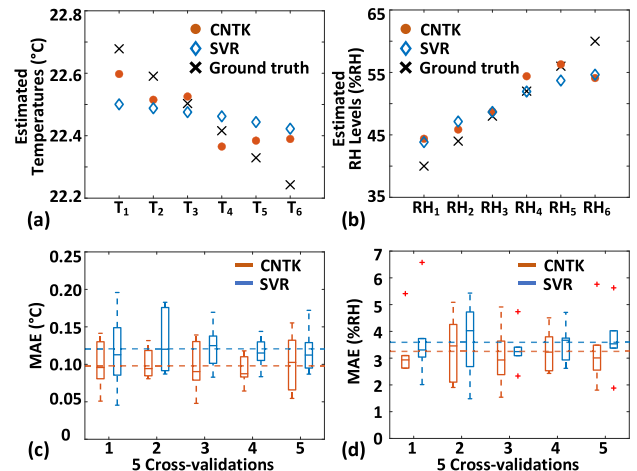


Fig. 12. CNTK-DL model and SVR-ML model were established with Dataset 3, which has degraded signal quality caused by strong noise, where the median values of estimated (a) temperatures and (b) RH levels by CNTK-DL model (red dots) still show a better precision than that by SVR-ML model (blue diamonds). The boxplot of MAE of (c) temperature and (d) humidity estimations in the five 6-fold cross-validations further demonstrate the better robustness and spectrum resolving power of the CNTK-DL model than that of the SVR-ML model. The dotted lines indicate the overall average MAE values.

indicating the excellent resistance of DL-based MWP sensing models to the laser drifts.

Finally, Dataset 3, with a high noise level, was employed for establishing the CNTK-DL and SVR-ML models to test their tolerance to signal degradation. The estimation results are shown in Fig. 12. In this case, the SVR-ML model remains an estimation performance similar to that with no additional interferences. Although the average MAEs of temperature and humidity estimation of CNTK-DL increase to around $0.10\text{ }^{\circ}\text{C}$ and 3.25% RH, respectively, they are still notably smaller than that of the SVR-ML model. This might be due to the fact that

the automatically extracted high-level features by the CNTK-DL model contain not only the dip position and power transmission that the SVR-ML model solely relies on but also other hidden features which can benefit the estimation but are now overwhelmed by the strong noise and interfered by the wide spectrum overlapping. This also suggests that increasing the size of the training dataset might be beneficial for the DL model to learn the features in a noisy environment. The higher estimation precision of the CNTK-DL model compared with that of the SVR-ML model, even in the strong noise situation, further indicates the benefit of conducting DL of the raw spectrum rather than relying on handcrafted features for sensing. As DL is a data-driven method capable of learning features automatically, by adopting a deeper neural network and training it with a large dataset involving all the possible environmental interferences, the resulting sensing model should achieve a higher capability level and preserve excellent performance in practical use.

V. CONCLUSION

In summary, we have proposed and demonstrated the use of DL to enable the MWP sensing of more than one measurand sensing with the minimum requirement on the number of optical resonances as well as the design and fabrication of optical microresonators. As a proof-of-concept, the proposed scheme is implemented in the simultaneous sensing of temperature and humidity via DL of the MWP interrogation result of a SOR of a PMMA-coated SOI MRR, where the CNTK is adopted as the DL model to reduce the demand on experimental data. The CNTK-DL model has been established and further evaluated in the presence of laser wavelength and power drifts and strong noise, respectively, in comparison with the SVR-ML model, which requires two handcrafted spectral features as the input. Despite the usage of a small dataset in training, the CNTK-DL model consistently outperforms the SVR-ML model, showing better robustness with high tolerance on the interference and noise and demonstrating nearly 2-fold and 3-fold higher accuracy with and without the interference of laser drift, respectively. Besides, within the system frequency range, the proposed sensor can be configured for any other measurand ranges by simply retraining the DL models with the MWP interrogation results collected in the new target range. With such low complexity in realizing the optical microresonator probe, the proposed MWP sensing scheme paves the way for the realization of cost-effective multi-parameter sensing and opens a new avenue for boosting the integrated optical sensing and the development of smart MWP sensors in which the complexity in hardware to combat cross-sensitivity or interference is shifted to software using the DL engine.

APPENDIX

The ML algorithm of SVR has been demonstrated to perform well in small dataset scenarios [34], [35], [52], [53]. For example, it outperformed the classification and regression trees [52] and the multi-layer perceptron neural network [53] when the size of the training data was even decreased to below thirty-six. The SVR by itself is designed to mitigate overfitting

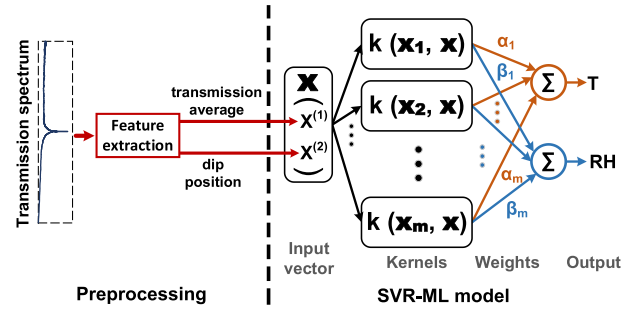


Fig. 13. Schematic diagram of the experimental SVR-ML approach that relies on two extracted spectral features to estimate the temperature (T) and relative humidity (RH).

via choosing a specific hyperplane via the max-margin criterion towards better model generalization, among many hyperplanes that can separate data in the feature space. To further mitigate overfitting for the small experimental datasets, the soft margin SVR, which allows a trade-off between maximizing the margin and minimizing the loss, is adopted. The SVR-ML approach for comparison purposes in the experiments is shown in Fig. 13. Unlike the CNTK-DL model that directly accepts the interrogation results as input, the SVR-ML model requires a preliminary procedure to extract the dip position and the transmission average of each transmission spectrum from the microwave photonic interrogation to constitute its input space. As the extension of the SVR model in our previous work [34], [35], the SVR-ML model in this work simultaneously predicts the temperature and humidity and no longer needs the DC bias voltages beyond the interrogation results, since the transmission average is dominated by the passband transmission off the resonance dip region, where the instantaneous transmitted power of the swept frequency signal is subject to the DC bias voltage of the modulator. The experimental SVR-ML model uses radial basis function kernel [54] to make the similarity comparison between the input vector and the support vectors in a sufficiently higher dimension, where the support vectors are the training samples around the ε tube [55] that determines a linear fitting function. The similarity tolerance is controlled by γ . The proportion of the number of points outside the ε tube is adjustable via the regularization parameter, C . After being multiplied by learnable weights α and β , the comparison results are then summed to be the estimated temperature and humidity, respectively. In the experiment, the hyperparameters of $\varepsilon = 0.1$, $C = 10$, and $\gamma = 2$ were determined in the preliminary validation process and used for the SVR-ML model.

ACKNOWLEDGMENT

Photonic waveguide fabrication and scanning electron microscopy were conducted at the Research and Prototype Foundry, a core research facility at the University of Sydney and a part of the Australian National Fabrication Facility. L. Li acknowledges the support of Sydney Research Accelerator Fellowship. X. Tian acknowledges the support of Research Training Program Scholarships from the University of Sydney.

REFERENCES

- [1] X. Jiang, A. J. Qavi, S. H. Huang, and L. Yang, "Whispering-gallery sensors," *Matter*, vol. 3, no. 2, pp. 371–392, 2020.
- [2] K. D. Heylman et al., "Optical microresonators for sensing and transduction: A materials perspective," *Adv. Mater.*, vol. 29, no. 30, 2017, Art. no. 1700037.
- [3] L. Li et al., "Processing, characterization, and impact of Nafion thin film on photonic nanowaveguides for humidity sensing," *Adv. Photon. Res.*, vol. 3, no. 2, 2022, Art. no. 2100181.
- [4] W. J. Westerveld et al., "Sensitive, small, broadband and scalable optomechanical ultrasound sensor in silicon photonics," *Nature Photon.*, vol. 15, no. 5, pp. 341–345, 2021.
- [5] S. Liu et al., "End-fire injection of light into high-Q silicon microdisks," *Optica*, vol. 5, no. 5, pp. 612–616, 2018.
- [6] B. B. Li et al., "Quantum enhanced optomechanical magnetometry," *Optica*, vol. 5, no. 7, pp. 850–856, 2018.
- [7] Y. N. Zhang, T. Zhou, B. Han, A. Zhang, and Y. Zhao, "Optical bio-chemical sensors based on whispering gallery mode resonators," *Nanoscale*, vol. 10, no. 29, pp. 13832–13856, 2018.
- [8] K. D. Heylman et al., "Optical microresonators as single-particle absorption spectrometers," *Nature Photon.*, vol. 10, no. 12, pp. 788–795, 2016.
- [9] X. Tian et al., "Cascaded optical microring resonator based auto-correction assisted high resolution microwave photonic sensor," *J. Light. Technol.*, vol. 39, no. 24, pp. 7646–7655, Dec. 2021.
- [10] H. Deng, W. Zhang, and J. Yao, "High-speed and high-resolution interrogation of a silicon photonic microdisk sensor based on microwave photonic filtering," *J. Light. Technol.*, vol. 36, no. 19, pp. 4243–4249, Oct. 2018.
- [11] X. Tian et al., "High-resolution optical microresonator-based sensor enabled by microwave photonic sidebands processing," *J. Light. Technol.*, vol. 38, no. 19, pp. 5440–5449, Oct. 2020.
- [12] S. X. Chew et al., "Optoelectronic oscillator based sensor using an on-chip sensing probe," *IEEE Photon. J.*, vol. 9, no. 2, Apr. 2017, Art. no. 5500809.
- [13] C. Y. Chao and L. J. Guo, "Design and optimization of microring resonators in biochemical sensing applications," *J. Light. Technol.*, vol. 24, no. 3, pp. 1395–1402, Mar. 2006.
- [14] I. M. White and X. Fan, "On the performance quantification of resonant refractive index sensors," *Opt. Exp.*, vol. 16, no. 2, pp. 1020–1028, 2008.
- [15] J. Capmany and D. Novak, "Microwave photonics combines two worlds," *Nature Photon.*, vol. 1, no. 6, 2007, Art. no. 319.
- [16] J. Capmany et al., "Microwave photonic signal processing," *J. Light. Technol.*, vol. 31, no. 4, pp. 571–586, Feb. 2013.
- [17] P. Ghelfi et al., "A fully photonics-based coherent radar system," *Nature*, vol. 507, no. 7492, pp. 341–345, 2014.
- [18] G. Serafino et al., "Microwave photonics for remote sensing: From basic concepts to high-level functionalities," *J. Light. Technol.*, vol. 38, no. 19, pp. 5339–5355, Oct. 2020.
- [19] S. Pan and Y. Zhang, "Microwave photonic radars," *J. Light. Technol.*, vol. 38, no. 19, pp. 5450–5484, Oct. 2020.
- [20] J. Hervás et al., "Microwave photonics for optical sensors," *IEEE J. Sel. Top. Quantum Electron.*, vol. 23, no. 2, pp. 327–339, Mar./Apr. 2017.
- [21] J. Yao, "Microwave photonic sensors," *J. Light. Technol.*, vol. 39, no. 12, pp. 3626–3637, Jun. 2020.
- [22] D. Marpaung, J. Yao, and J. Capmany, "Integrated microwave photonics," *Nature Photon.*, vol. 13, no. 2, pp. 80–90, 2019.
- [23] J. Liu, H. Deng, W. Zhang, and J. Yao, "On-chip sensor for simultaneous temperature and refractive index measurements based on a dual-passband microwave photonic filter," *J. Light. Technol.*, vol. 36, no. 18, pp. 4099–4105, Sep. 2018.
- [24] Y. LeCun, Y. Bengio, and G. Hinton, "Deep learning," *Nature*, vol. 521, no. 7553, pp. 436–444, 2015.
- [25] L. Zhang, L. Zhang, and B. Du, "Deep learning for remote sensing data: A technical tutorial on the state of the art," *IEEE Trans. Geosci.*, vol. 4, no. 2, pp. 22–40, Jun. 2016.
- [26] L. V. Nguyen, C. C. Nguyen, G. Carneiro, H. Ebendorff-Heidepriem, and S. C. Warren-Smith, "Sensing in the presence of strong noise by deep learning of dynamic multimode fiber interference," *Photon. Res.*, vol. 9, no. 4, pp. B109–B118, 2021.
- [27] B. Wang et al., "Deep neural networks assisted BOTDA for simultaneous temperature and strain measurement with enhanced accuracy," *Opt. Exp.*, vol. 27, no. 3, pp. 2530–2543, 2019.
- [28] J. A. Grant-Jacob et al., "Real-time particle pollution sensing using machine learning," *Opt. Exp.*, vol. 26, no. 21, pp. 7237–7246, 2018.
- [29] A. V. Saetchnikov, E. A. Tcherniavskaia, V. A. Saetchnikov, and A. Ostendorf, "Deep-learning powered whispering gallery mode sensor based on multiplexed imaging at fixed frequency," *Opto-electron. Adv.*, vol. 3, no. 11, 2020, Art. no. 200048.
- [30] Z. Li et al., "Smart ring resonator-based sensor for multicomponent chemical analysis via machine learning," *Photon. Res.*, vol. 9, no. 2, pp. B38–B44, 2021.
- [31] A. V. Saetchnikov, E. A. Tcherniavskaia, V. A. Saetchnikov, and A. Ostendorf, "Intelligent optical microresonator imaging sensor for early stage classification of dynamical variations," *Adv. Photon. Res.*, vol. 2, no. 12, 2021, Art. no. 2100242.
- [32] B. Duan et al., "High-precision whispering gallery microsensors with ergodic spectra empowered by machine learning," *Photon. Res.*, vol. 10, no. 10, pp. 2343–2348, 2022.
- [33] M. A. Jabin and M. P. Fok, "Prediction of 12 photonic crystal fiber optical properties using MLP in deep learning," *IEEE Photon. Technol. Lett.*, vol. 34, no. 7, pp. 391–394, Apr. 2022.
- [34] G. Gunawan et al., "Machine learning assisted temperature insensitive microwave photonic sensor based on single microring resonance," in *Proc. IEEE Int. Topical Meeting Microw. Photon.*, 2021, pp. 1–4.
- [35] X. Tian et al., "Athermal microwave photonic sensor based on single microring resonance assisted by machine learning," *J. Light. Technol.*, vol. 40, no. 20, pp. 6796–6804, Oct. 2022.
- [36] J. Lu et al., "Experimental demonstration of multimode microresonator sensing by machine learning," *IEEE Sens. J.*, vol. 21, no. 7, pp. 9046–9053, Apr. 2021.
- [37] C. Janiesch, P. Zschech, and K. Heinrich, "Machine learning and deep learning," *Electron. Marketing.*, vol. 31, no. 3, pp. 685–695, 2021.
- [38] R. Brehar et al., "Comparison of deep-learning and conventional machine-learning methods for the automatic recognition of the hepatocellular carcinoma areas from ultrasound images," *Sensors*, vol. 20, no. 11, 2020, Art. no. 3085.
- [39] S. Dargan, M. Kumar, M. R. Ayyagari, and G. Kumar, "A survey of deep learning and its applications: A new paradigm to machine learning," *Arch. Comput. Methods Eng.*, vol. 27, no. 4, pp. 1071–1092, 2020.
- [40] W. Bogaerts et al., "Silicon microring resonators," *Laser Photon. Rev.*, vol. 6, no. 1, pp. 47–73, 2012.
- [41] K. Okamoto, "Planar optical waveguides," in *Fundamentals of Optical Waveguides*. Amsterdam, Netherlands: Elsevier, 2021, pp. 13–66.
- [42] X. Tian, L. Li, L. Nguyen, R. Minasian, and X. Yi, "Automatic correction assisted microwave photonic sensor system for resolution enhancement in humidity measurement," in *Proc. IEEE Int. Topical Meeting Microw. Photon.*, 2020, pp. 66–69.
- [43] K. Padmaraju and K. Bergman, "Resolving the thermal challenges for silicon microring resonator devices," *Nanophotonics*, vol. 3, no. 4–5, pp. 269–281, 2014.
- [44] T. Watanabe, N. Ooba, Y. Hida, and M. Hikita, "Influence of humidity on refractive index of polymers for optical waveguide and its temperature dependence," *Appl. Phys. Lett.*, vol. 72, no. 13, pp. 1533–1535, 1998.
- [45] S. Arora et al., "Harnessing the power of infinitely wide deep nets on small-data tasks," in *Proc. Int. Conf. Learn. Representations*, 2020, pp. 1–6.
- [46] S. Arora et al., "On exact computation with an infinitely wide neural net," in *Proc. Adv. Neural Inf. Process. Syst.*, 2019, pp. 8139–8148.
- [47] Z. Li et al., "Enhanced convolutional neural tangent kernels," 2019, *arXiv:1911.00809*.
- [48] Y. Bai, B. Krause, H. Wang, C. Xiong, and R. Socher, "Taylorized training: Towards better approximation of neural network training at finite width," 2020, *arXiv:2002.04010v2*.
- [49] J. B. Simon, M. Dickens, and M. R. DeWeese, "The eigenlearning framework: A conservation law perspective on kernel regression and wide neural networks," 2023, *arXiv:2110.03922v5*.
- [50] R. Novak et al., "Neural tangents: Fast and easy infinite neural networks in python," in *Proc. Int. Conf. Learn. Representations*, 2020, pp. 1–6.
- [51] S. Song, S. X. Chew, L. Nguyen, and X. Yi, "High-resolution microwave frequency measurement based on dynamic frequency-to-power mapping," *Opt. Exp.*, vol. 29, no. 26, pp. 42553–42568, 2021.
- [52] C. Ballabio, "Spatial prediction of soil properties in temperate mountain regions using support vector regression," *Geoderma*, vol. 151, no. 3–4, pp. 338–350, 2009.
- [53] A. F. Al-Anazi and I. D. Gates, "Support vector regression to predict porosity and permeability: Effect of sample size," *Comput. Geosci.*, vol. 39, pp. 64–76, 2012.

- [54] S. Han, C. Qubo, and H. Meng, "Parameter selection in SVM with RBF kernel function," in *Proc. World Automat. Congr.*, 2012, pp. 1–4.
- [55] M. Awad and R. Khanna, "Support vector regression," in *Efficient Learning Machines*. Berkeley, CA, USA: Apress, 2015, pp. 67–80.

Xiaoyi Tian received the B.Sc. degree in engineering and the M.Sc. degree in information and communication engineering from Shanghai Jiao Tong University, Shanghai, China, in 2014 and 2017, respectively, and the Ph.D. degree in engineering from The University of Sydney, Sydney, NSW, Australia, in 2022. He is currently a Postdoctoral Research Associate with the School of Electrical and Information Engineering, The University of Sydney. His research interests include microwave photonic signal processing, integrated photonics, and sensing.

Luping Zhou (Senior Member, IEEE) received the Ph.D. degree from Australian National University, Canberra, ACT, Australia. She is currently an Associate Professor with the School of Electrical and Information Engineering, University of Sydney, Sydney, NSW, Australia. Her research interests include machine learning, medical image analysis, and computer vision. She was the recipient of Australian Research Council DECRA Award (Discovery Early Career Researcher Award) in 2015.

Liwei Li (Member, IEEE) received the B.E. (with First Class Hons.) and Ph.D. degrees in electrical engineering from the University of Sydney, Sydney, NSW, Australia, in 2009 and 2013, respectively. She is currently a Senior Lecturer with the School of Electrical and Information Engineering, University of Sydney. Her research interests include microwave photonics, photonic signal processing and sensing, optical communication systems, lightwave technology, and fibre-optic communications.

Giorgio Gunawan received the B.E. degree from the School of Aerospace, Mechanical and Mechatronic Engineering, University of Sydney, Sydney, NSW, Australia.

Linh Nguyen received the B.Sc. and B.E. (with First Class Hons.) degrees from the University of Adelaide, Adelaide SA, Australia, in 1992 and 1993, respectively, and the Ph.D. degree in electrical and electronic engineering from the University of Melbourne, Parkville, VIC, Australia, in 1997. He is currently collaborating with the School of Electrical and Information Engineering, University of Sydney, Sydney, NSW, Australia, as an Adjunct Professor. His research interests include microwave photonics for signal processing and sensing.

Xiaoke Yi (Member, IEEE) received the Ph.D. degree from Nanyang Technological University, Singapore, in 2004. She is currently a Professor with the School of Electrical and Information Engineering, University of Sydney, Sydney, NSW, Australia. She was the First Cohort of Sydney Research Accelerator Fellow with the University of Sydney. From 2011 to 2017, she was an Australian Research Council QEII Fellow. Her main research interests include photonic signal processing, microwave photonics, integrated photonics, sensors and phased-array antennas. She is the Fellow of the Royal Society of NSW.